

Large Anomalous Hall Effect at Room Temperature in a Fermi-Level-Tuned Kagome Antiferromagnet

Linxuan Song, Feng Zhou, Hang Li, Bei Ding, Xue Li, Xuekui Xi, Yuan Yao, Yong-Chang Lau, and Wenhong Wang*

The recent discoveries of surprisingly large anomalous Hall effect (AHE) in antiferromagnets have attracted much attention due to their promising use in spintronics devices. However, such AHE-hosting antiferromagnetic materials are rare in nature. Herein, it is demonstrated that $\text{Mn}_{2.4}\text{Ga}$, a Fermi-level-tuned kagome antiferromagnet, has a large anomalous Hall conductivity of $\approx 150 \Omega^{-1} \text{cm}^{-1}$ at room temperature that surpasses the usual high values (i.e., $20\text{--}50 \Omega^{-1} \text{cm}^{-1}$) observed so far in two outstanding kagome antiferromagnets, Mn_3Sn and Mn_3Ge . Although the triangular spin structure of $\text{Mn}_{2.4}\text{Ga}$ shows a weak net magnetic moment of $\approx 0.05 \mu_B$ per formula unit, it guarantees a nonzero Berry curvature in the kagome plane. Moreover, the anomalous Hall conductivity exhibits a sign reversal with the rotation of a small magnetic field that can be ascribed to the field-controlled chirality of the spin triangular structure. This theoretical calculations further suggest that the large AHE in $\text{Mn}_{2.4}\text{Ga}$ originates from a significantly enhanced Berry curvature associated with the tuning of the Fermi level close to the Weyl points. These properties, together with the ability to manipulate moment orientations using a moderate external magnetic field, make $\text{Mn}_{2.4}\text{Ga}$ extremely exciting for future antiferromagnetic spintronics.

correlated topological electronic structures.^[8–15] In addition, this trend has also triggered renewed attention in understanding the mechanism of the anomalous Hall effect (AHE) observed in ferromagnetic conductors, which is the spontaneous transverse voltage drop induced by a longitudinal electric current.^[16] The AHE has been considered to be proportional to the magnetization, and thus observed only in magnetic materials.^[17,18] In contrast, the recent theoretical and experimental advances have demonstrated that the sizable AHE can be realized in materials with nearly zero magnetization, such as spin liquids and chiral antiferromagnets, if a nonzero Berry curvature is guaranteed in the momentum-space.^[19–22] One of the most important findings is the surprisingly large AHE observed at room temperature in the hexagonal antiferromagnets Mn_3Sn (space group $P6_3/mmc$), in which all the Mn atoms form a kagome lattice in the $x\text{--}y$ plane.^[23] When cooled below its Néel temperature of 430 K, the

Mn magnetic moments form an inverse triangular spin configuration, yielding a nonzero Berry curvature and producing a weak net magnetization with small magnetic anisotropy within the kagome plane. These unique properties make the antiferromagnetic structure of Mn_3Sn easily switchable via various external stimulants, such as magnetic fields, spin-polarized currents, and a uniaxial strain.^[24–27]

Shortly after the discovery of the large AHE in Mn_3Sn , another kagome-based antiferromagnet Mn_3Ge , isostructural to Mn_3Sn , was also reported to show a large anomalous Hall conductivity of $\approx 50 \Omega^{-1} \text{cm}^{-1}$ at room temperature.^[28,29] In addition to the large AHE, other unique anomalous thermal, optical, and topological transport responses, such as the large anomalous Nernst effect (ANE), the planar Hall effect (PHE), and the topological Hall effect, have subsequently been observed in Mn_3Sn and Mn_3Ge , due to spin chirality induced a large Berry curvature by gapping the Weyl nodal lines.^[30–36] In particular, a field-induced linear AHE has recently been reported in Mn_3Sn , arising from the large Berry curvature on the Fermi surface.^[27] Nevertheless, the large AHE has thus far only been reported in the above-mentioned two kagome-based antiferromagnets Mn_3Sn and Mn_3Ge , and more recently in a non-kagome based non-collinear antiferromagnet YbMnBi_2 .^[37] Therefore, the search for new kagome-based

1. Introduction

Kagome-based materials with topologically nontrivial electronic structures have attracted tremendous interest in the past decade in the fields of condensed-matter physics and materials science.^[1–7] Recently, a series of kagome-based ferromagnets have been observed to show anomalous transport response, topological magnetic textures, large spin-orbit tunability, and

L. Song, F. Zhou, H. Li, B. Ding, X. Li, X. Xi, Y. Yao, Y.-C. Lau, W. Wang
Institute of Physics
Chinese Academy of Sciences
Beijing 100190, China
E-mail: wenhong.wang@iphy.ac.cn

F. Zhou, H. Li, W. Wang
School of Electronics and Information Engineering
Tiangong University
Tianjin 300387, China

X. Li, Y.-C. Lau
University of Chinese Academy of Sciences
Beijing 100049, China

The ORCID identification number(s) for the author(s) of this article can be found under <https://doi.org/10.1002/adfm.202316588>

DOI: 10.1002/adfm.202316588

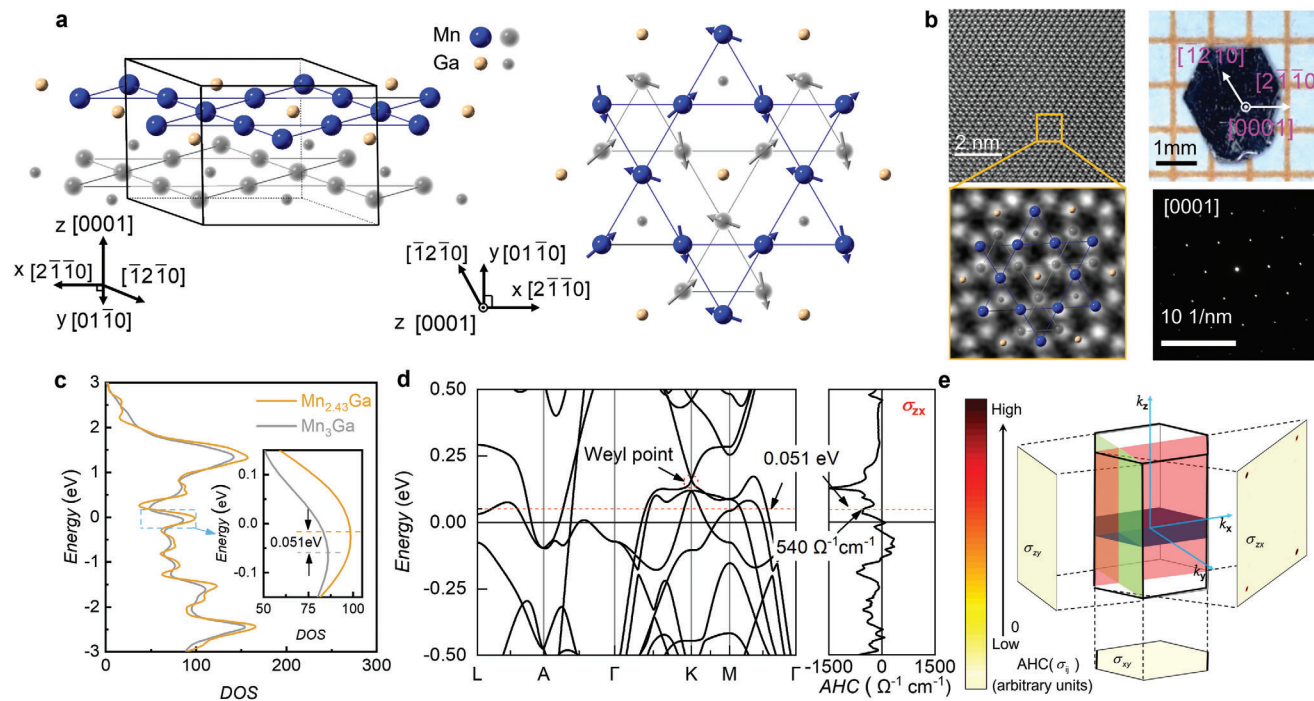


Figure 1. Crystal magnetic and electronic structures. a) The crystallographic unit cell of Mn₃Ga. In each unit cell, two layers Mn–Ga atoms are stuck along z [0001] direction. Small and big spheres represent Ga and Mn atoms, respectively. The colored and gray balls represent the top and bottom layers, respectively. The kagome lattice in x-y plane is shown in the right panel. The Mn moments of each triangular lattice in the x-y plane form the noncollinear antiferromagnetic configuration. b) High-resolution STEM images (left) along the [0001] directions of single crystal Mn_{2.4}Ga. The SAED pattern is shown in the bottom right corner to confirm the direction. The optical photograph is shown in the top right corner. c) Total density of states of the Mn₃Ga and Mn_{2.43}Ga. d) Band structure and anomalous Hall conductivity σ_{zx} of the Mn₃Ga. The red dash line shows the Fermi level shift for Ga-rich Mn_{2.4}Ga. e) First Brillouin zone and momentum-dependent AHC of Mn₃Ga. The σ_{ij} is the component of the AHC tensor in the k_i - k_j plane, corresponding to the Berry curvature of all occupied electronic states integrated over the k_k direction ($k \parallel i \times j$).

antiferromagnets with large AHE is of considerable importance, which will broaden the material platform for future antiferromagnetic spintronics as well as for in the search for novel topological phenomena.

Here we report on the first experimental realization of the long-sought-after last member of the Mn₃X kagome antiferromagnet family, off-stoichiometric Mn₃Ga (Mn_{2.4}Ga) in the form of single crystals which shows the large anomalous Hall conductivity by tuning the Fermi level close to the Weyl points. We show that, although a small magnetization of $\approx 0.05 \mu_B$ per formula unit in the kagome plane, the single crystal of Mn_{2.4}Ga exhibits a large anomalous Hall conductivity of $\approx 150 \Omega^{-1} \text{cm}^{-1}$ at room temperature and $\approx 530 \Omega^{-1} \text{cm}^{-1}$ at 10 K. The angular dependence of the AHE measurements further confirms that the small residual in-plane magnetization can switch the chirality of the spin triangular structure. Moreover, our detailed band structure calculations indicate that the large AHE in Mn_{2.4}Ga originates from a significantly enhanced Berry curvature associated with the tuning of the Fermi level close to the Weyl points.

2. Results and Discussion

The manganese-based binary alloys Mn_{3-x}Ga are known to crystallize in different structures such as cubic, tetragonal, and hexagonal phases, depending on the annealing temperature and the

composition.^[38–51] Among them, the hexagonal phase exists in the range of Mn_{2.35}Ga–Mn_{2.8}Ga and exhibits a layered kagome antiferromagnetic structure with an ordering temperature of $T_N \sim 430$ to 480 K (Figure S1, Supporting Information). As shown in Figure 1a, the hexagonal-structured Mn₃Ga, similar to Mn₃Sn and Mn₃Ge, consists of bi-layer of Mn triangles arranged along the c-axis. In each layer, the Mn atoms constitute a slightly distorted kagome lattice with Ga located at the center of a hexagon. The structure is only stable in the case of excess Ga randomly occupying the Mn sites.^[38] Below its ordering temperature, the Mn moments form a noncollinear triangular antiferromagnetic structure. In this structure, neighboring Mn moments lie in the x-y plane at an angle of 120° (Figure 1b), as previously revealed by neutron diffraction studies.^[39] It should be noted that, to date, there are only scarce studies on polycrystalline hexagonal Mn₃Ga and no report on the properties of single crystals, possibly due to the complicated Mn–Ga binary phase diagram,^[52] which hinders the growth of stoichiometric hexagonal Mn₃Ga in equilibrium state. To the best of our knowledge, the topological Hall effect and the large piezospinronic effect have only been observed in polycrystalline stoichiometric Mn₃Ga in bulk and thin film forms, respectively.^[53,54] In this study, we have successfully grown high-quality single crystals of non-stoichiometric Mn_{2.4}Ga (Figure S2, Supporting Information). Using single-crystal X-ray diffraction (XRD), it has been confirmed that Mn_{2.4}Ga has a Ni₃Sn-type hexagonal structure with space group P6₃/mmc. The

extracted lattice parameters are as follows: $a = 5.4135(8)$ Å, $c = 4.3605(9)$ Å, and $\alpha = 90$, $\beta = 120^\circ$. The temperature dependence of the magnetization M (T) indicates a T_N of 435 K for the single crystals of $Mn_{2.4}Ga$. These parameters are in good agreement with those detected in polycrystalline $Mn_{2.4}Ga$ (Figure S1, Supporting Information). The high-quality crystal structure was further confirmed by our high-resolution scanning transmission electron microscopy (STEM) and selected-area electron diffraction (SAED) shown in Figure 1b. According to the structural model obtained by single crystal XRD, the zone axes of the SAED patterns can be identified as [0001] direction (c-axis). The high-resolution-STEM image taken along the [0001] direction can be perfectly overlaid with the structural model, verifying that the index of the SAED patterns is self-consistent and thus the crystal orientations are successfully indexed.

2.1. Band Structures and Berry Curvatures

We have performed the electronic band structure calculations of Mn_3Ga , which are consistent with previous calculations.^[55] As shown in Figure 1c, the calculated total density of states of the Mn_3Ga and $Mn_{2.43}Ga$ shows a peak shift of ≈ 0.051 eV, which indicates the Fermi level (E_F) will move up. The band structures show little difference except for the Fermi level shifts between the Mn_3Ga and $Mn_{2.43}Ga$ (Figure S4, Supporting Information). In both cases, when spin-orbit coupling (SOC) is included, the nodal line is gapped, leading to two pairs of Weyl points and a nonzero Berry curvature. The value of the Berry curvature depends on the position of the E_F , and reaches its maximum when the E_F is approaching to the Weyl points. From these band structure calculations, we highlight that, although the stoichiometric Mn_3Ga has a very small AHC, a large AHC may be produced in the non-stoichiometric $Mn_{2.4}Ga$ due to the E_F shift being close to the Weyl points. For comparison, in Figure 1d, we show the calculated AHC of Mn_3Ga . One can see that the AHC for z - x (σ_{zx}) component is nearly zero for Mn_3Ga , whereas this value reaches up to $540 \Omega^{-1} \text{ cm}^{-1}$ (for $Mn_{2.43}Ga$, due to the E_F shifted up approaching to the Weyl points). Indeed, this value of $540 \Omega^{-1} \text{ cm}^{-1}$ in $Mn_{2.43}Ga$ is very large and exceeds the other two Kagome-based antiferromagnets Mn_3Sn and Mn_3Ge . Here, σ_{ij} refers to the AHC, in which the current flows along the j and the Hall voltage along the i directions, respectively.

The anisotropy of AHC for Mn_3Ga , i.e., σ_{zx} in the x - z plane, σ_{zy} in the y - z plane, and σ_{xy} in the x - y plane are further calculated, and the results are shown in Figure 1e. We found that only the σ_{zx} shows the stronger AHC, while the σ_{zy} and σ_{xy} are nearly zero, which is consistent with the previous calculations of the Mn_3Sn and Mn_3Ge demonstrated that σ_{zy} and σ_{xy} should be zero due to the mirror symmetry of antiferromagnetic structure with respect to the x - z plane.^[29,55] It should be noted that, in Mn_3Ge and Mn_3Sn , the experimental non-zero value of σ_{zy} can be attributed to the perturbation of the mirror symmetry caused by the non-zero moment in the kagome plane. In this sense, we predicted that similar to Mn_3Ge and Mn_3Sn , the non-stoichiometric $Mn_{2.4}Ga$ may show a large AHE and also a strong anisotropy AHC experimentally.

2.2. Large Anomalous Hall effect

We first provide clear evidence of the large AHE observed in single crystals of $Mn_{2.4}Ga$. All the transport measurements were performed on Hall devices with $\approx 15 \mu\text{m} \times 7 \mu\text{m} \times 1 \mu\text{m}$ channels for longitudinal and Hall resistivity measurements (see Experiment Section and Figure S5, Supporting Information). Figure 2a shows the magnetic field H dependence of the Hall resistivity ρ_{zx} for the current I along [2-1-10] and H parallel to [01-10], namely, H is parallel to the kagome plane (which we label as configuration I). Obviously, the ρ_{zx} curve exhibits a clear hysteresis loop with a sharp jump and attains a large saturation value of $\approx 2 \mu\Omega\text{-cm}$ at 300 K and $\approx 5.9 \mu\Omega\text{-cm}$ at 10 K. In other words, a large remanent Hall effect at zero field is observed in configuration I and suggests that these Hall devices are mostly a single AFM domain. Here we define the x , y , and z coordinates along [2-1-10], [01-10], and [0001] directions, and then estimate the anomalous Hall conductivity (AHC) for comparison with theoretical values. As shown in Figure 2d, the AHC for the configuration I (σ_{zx}), calculated from $\sigma_H = -\rho_H/\rho^2$, (where ρ is the longitudinal resistivity), shows a large value of $\approx 150 \Omega^{-1} \text{ cm}^{-1}$ at 300 K, and reaches $\approx 530 \Omega^{-1} \text{ cm}^{-1}$ at 10 K, which is quite high, especially for an antiferromagnet. Remarkably, the large AHC of $\approx 150 \Omega^{-1} \text{ cm}^{-1}$ at 300 K, to the best of our knowledge, surpasses the high values observed in $Mn_3Sn \approx 20 \Omega^{-1} \text{ cm}^{-1}$ and $Mn_3Ge \approx 50 \Omega^{-1} \text{ cm}^{-1}$.

To study the anisotropic behavior of AHE, we have measured ρ_{zy} with I along [01-10] and H parallel to [2-1-10]. In this configuration, H is still parallel to the kagome plane. As shown in Figure 2b, the ρ_{zy} is slightly smaller than configuration I ($\approx 5.1 \mu\Omega\text{-cm}$ at 10 K and $1.6 \mu\Omega\text{-cm}$ at 300 K). In contrast, σ_{zy} is significantly reduced down to $\approx 220 \Omega^{-1} \text{ cm}^{-1}$ at 10 K in configuration II compared to configuration I, while a modest value of $\sigma_H = 45 \Omega^{-1} \text{ cm}^{-1}$ at 300 K is found for configuration II (Figure 2e). For comparison, in configuration III, we apply I along [2-1-10] and H parallel to [0001], namely H is perpendicular to the kagome plane. In this configuration, both ρ_{xy} and σ_{xy} show no hysteresis but only a nearly linear field dependence at all temperatures, as shown in Figure 2c-f, respectively. The more detailed results can be found in Figures S6-S9 (Supporting Information).

Notably, the experimental results are highly consistent with the theoretical predictions: large AHE are observed in σ_{zx} and σ_{zy} , but not in σ_{xy} . Therefore, the nonzero Berry curvature related to the noncollinear antiferromagnetism is believed to be responsible for AHE. It should be noted that the reliability of the experimental protocols was further confirmed by the Mn_3Sn single-crystal devices fabricated using the same microfabrication method, thus an artificial AHE signals due to thickness variation, defects, and interface modification can be safely excluded in this work. A detailed analysis of the AHE can be found in Figures S10 and S11 (Supporting Information). Furthermore, we experimentally verified that the sign of the AHC is the same for non-stoichiometric $Mn_{2.4}Ga$ and Mn_3Sn , which is in line with theoretical calculations.^[30,55]

2.3. In-Plane Weak Ferromagnetism

To confirm that the observation of a large AHE originates from the noncollinear antiferromagnetic spin structure in the kagome

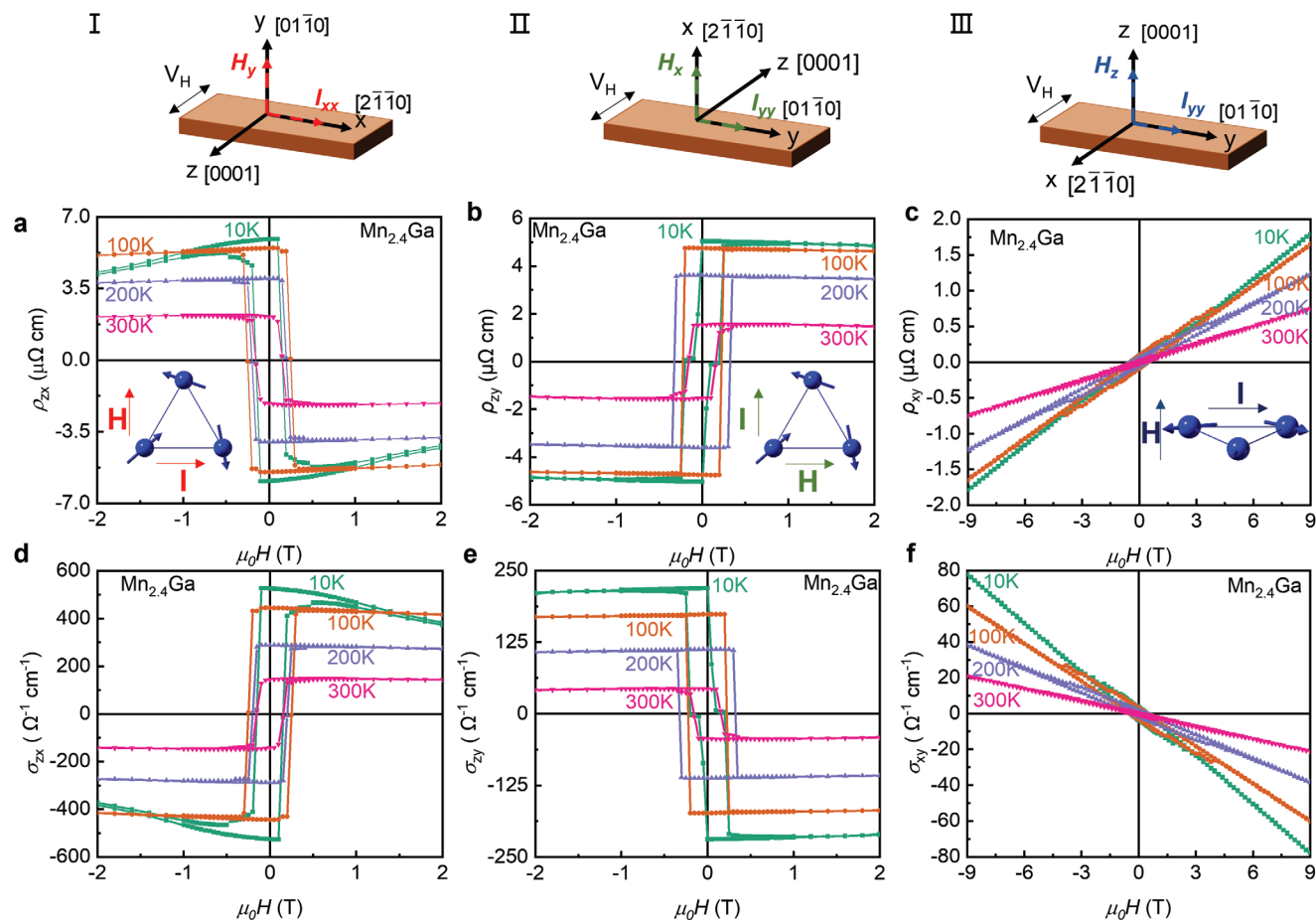


Figure 2. Magnetic field dependence of AHE in $\text{Mn}_{2.4}\text{Ga}$. a–c) Field dependence of the Hall resistivity ρ_H and d–f), Field dependence of the AHC measured at various temperatures with three different current and magnetic field configurations: the magnetic field $H\parallel y$ with the electric current $I\parallel x$ (configuration I), $H\parallel x$, $I\parallel y$ (configuration II) and $H\parallel z$, $I\parallel y$ (configuration III). The configurations are illustrated above the corresponding data. The triangular spin structures were shown in the inserts to further indicate the measurement configurations.

plane, we have performed magnetization measurements with the field parallel to different crystallographic directions. **Figure 3a** shows the temperature dependence of magnetization of $\text{Mn}_{2.4}\text{Ga}$ with the field parallel to the x, y, and z directions, respectively. The ordering temperature of $T_N \sim 435$ K is consistent with data for polycrystals. In addition, the magnetization curves show anisotropic hysteresis similar to that found for the Hall effect. For example, as shown in **Figure 3b**, the M–H loops measured with the field parallel to the in-plane $[01\bar{1}0]$ (y) direction at temperatures between 10 and 400 K shows clear hysteresis, indicating that a weak spontaneous magnetization of $0.002\text{--}0.05 \mu_B$ per formula unit. When the field is applied parallel to the in-plane $[2\bar{1}\bar{1}0]$ (x) direction, as shown in **Figure 3c**, the magnetization is almost isotropic in the Kagome plane and the zero field moment is slightly smaller ($0.04 \mu_B$ per formula unit at 10 K). A clear magnetic hysteresis with coercive fields (H_C) of less than 0.05 T can be found in both cases. Although the magnetic moments of Mn atoms are arranged within the ab plane when the field is applied parallel to the $[0001]$ direction (c-axis), we obtain a very small magnetization at 10 K. This indicates that the Mn spins have a very small tilting toward the c-axis. The magnetization curves measured at 300 K for different field orientations are similar to the

10 K data and show almost linear dependence behavior at higher fields (**Figure 3d**).

Based on our magnetization data, it is evident that the present kagome-based $\text{Mn}_{2.4}\text{Ga}$ antiferromagnet has a weak in-plane ferromagnetism and nearly zero net magnetic moment along $[0001]$ (z) direction. We thus argue that the weak in-plane ferromagnetism occurs due to the Mn spins arranged in a triangular noncollinear configuration in the x-y plane. Such configuration is robust against an external field of up to 16 T (inset **Figure 3d**). Hence, it can be concluded that the large AHE observed in the field parallel to the kagome plane (**Figure 2a,b**) must be related to the triangular noncollinear spin structures. In this case, the results of magnetization are well agreed with the AHE measurements. Moreover, a large AHC observed in both the x-z and the y-z planes is also consistent with symmetry analysis.

It should be pointed out that all antiferromagnet kagome Mn_3X alloys are off-stoichiometry triangular antiferromagnet. The hexagonal Mn_3Ga can be only stabilized with the Ga-rich compositions,^[39] while the Mn_3Sn and Mn_3Ge can be only obtained with the excessive Mn.^[30,56] The neutron diffraction experiments have confirmed the noncollinear antiferromagnetic structure for these alloys, assuming that the excess atoms randomly

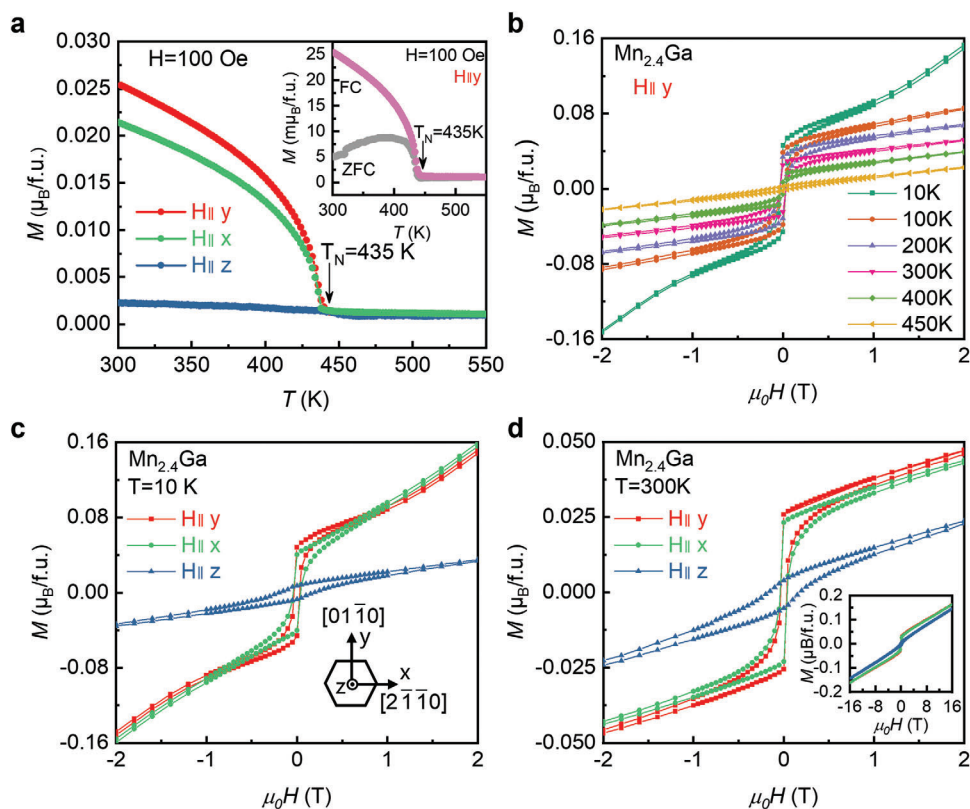


Figure 3. Magnetic properties of $\text{Mn}_{2.4}\text{Ga}$. a) The temperature dependence of the magnetization (M – T) with 100 Oe applied along the y , x , and z axes, respectively. The inset shows the zero field cooling and the field cooling M – T curves with 100 Oe applied along y axis. b) Magnetic field dependence of the magnetization (M – H) with field H || y at different temperatures between 10 and 400 K. c,d) Field dependence of the magnetization with magnetic field applied along y , x , and z , at 10 and 300 K, respectively. Inset in (d) shows the high magnetic field M – H curves up to 16 T with magnetic field applied along y , x , and z , at 300 K.

occupy the deficiencies.^[39,57] In $\text{Mn}_{2.4}\text{Ga}$, $\approx 5.9\%$ of Mn vacancies were occupied by Ga atoms. While, in Mn_3Sn , $\approx 6\%$ – 9% Sn atom sites are occupied by Mn atoms,^[30,36] and in Mn_3Ge $\approx 3.6\%$ – 13% Ge atom sites are occupied by Mn atoms.^[28,36] However, the polarized neutron diffraction experiments indicate that the weak magnetism in Mn_3Sn mainly originates from the triangular structure and not the excess concentration of Mn which can induce the uncompact magnetic state.^[58] This finding is also supported by the M – H curves of the Mn_3X alloys, which demonstrate that the weak ferromagnetism solely appears in the kagome plane. Most importantly, experiments and theoretical calculations have confirmed that weak ferromagnetism does not play a role in the AHE in Mn_3Sn ^[55] and Mn_3Ge .^[29] Though the theoretical calculations have already confirmed this point in $\text{Mn}_{2.4}\text{Ga}$, we also performed the following experiments to verify it.

2.4. Angular Dependence AHE

To confirm that the weak in-plane magnetization observed in $\text{Mn}_{2.4}\text{Ga}$ does no effect on the large AHE, we performed angular dependence of AHE measurements for various configurations of magnetic field H and current I . Below, we will demonstrate how drastically the AHC in $\text{Mn}_{2.4}\text{Ga}$ depends on the measurement configuration. **Figure 4a** shows the configuration I, in which we

applied the current along x -axis and measured the Hall voltage V_H within the z - x plane. In this configuration, the magnetic field is first applied along y , $\theta = 0$. We then rotate the field within the y - z plane. Interestingly, the value of σ_{zy} remains almost unchanged until $\theta = 90^\circ$, where it abruptly changes sign. With increasing θ , a second sign change happens again at $\theta = 270^\circ$. In configuration II shown in **Figure 4b**, the current was applied along y and the Hall voltage V_H is measured in the z - y plane, while the field is rotated within the x - z plane. In configuration I and configuration II, the rotating field is always perpendicular to the current and the x - y Kagome plane. We found that the angular dependence of the σ_{zy} shows the same inclination as that of configuration I. In both cases, a nearly constant AHC was observed as long as a small field was applied parallel to the in-plane kagome planes, with the exception of the abrupt sign change at $\theta = 90^\circ$ and 270° . This behavior can be explained as follows: with increasing θ , a small component of the in-plane magnetic field remains parallel to the kagome planes up to $\theta = 90^\circ$, which is capable of preserving the chirality of the in-plane triangular spin structure. However, at $\theta > 90^\circ$, the component of in-plane field changes its direction and causes a change in the chirality of the spin structure, resulting in the sign change of the AHC. A similar mechanism occurs at $\theta = 270^\circ$ in both configuration I and configuration II. In contrast, in configuration III shown in **Figure 4c**, if the field was rotated within the z - x plane, and the Hall voltage V_H was

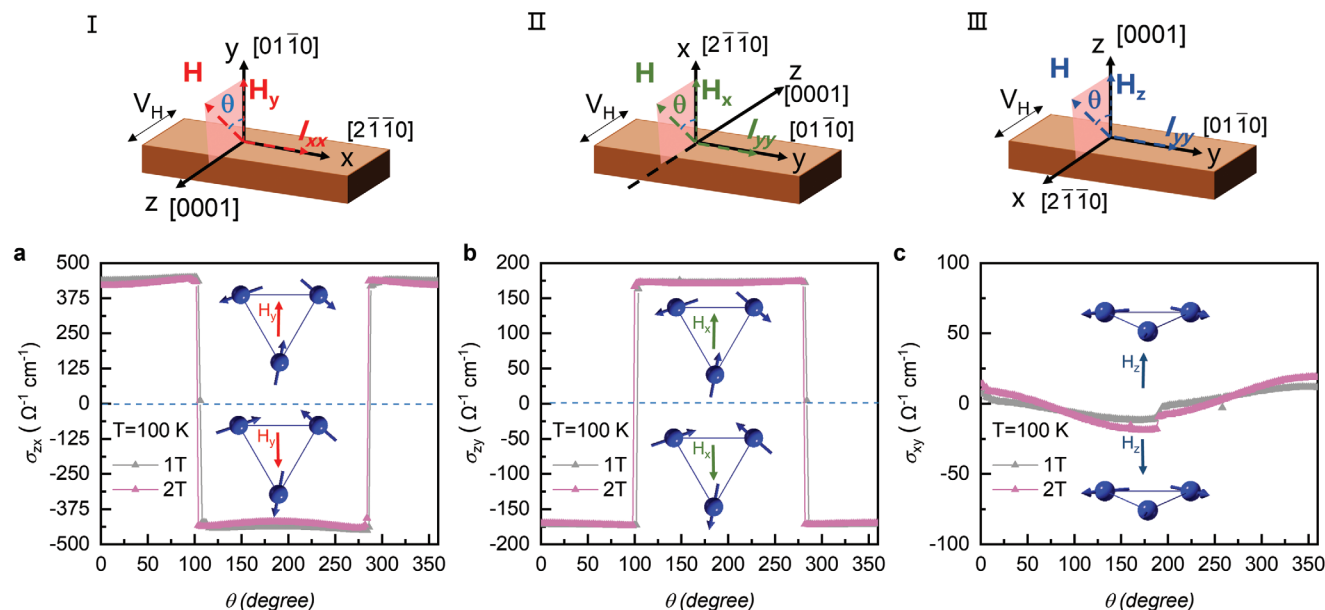


Figure 4. Angular dependence of AHE for single crystal $\text{Mn}_{2.4}\text{Ga}$. Angular (θ) dependence of the AHC in three fields and current configurations which are shown by the schematic diagram above the corresponding data. The field was rotated within the y - z plane for I along x (configuration I) a) x - z plane for I along y , (configuration II) b), x - y plane for I along y (configuration III) c), respectively. Two typical magnetic fields of 1 T (black line) and 2 T (purple line) were applied at $T = 100$ K. $\theta = 0^\circ$ corresponds to the magnetic field oriented along y , x , and z respectively. The insets show the changes in triangular spin chirality induced by the three magnetic field components H_y , H_x , and H_z , respectively.

measured in the x - y plane with I along y . In this configuration, the component of the magnetic field is always parallel to the kagome plane, except for $\theta = 0$ and 180° . As a result, the AHC measured in the x - y plane (σ_{xy}) is always negligibly small, which may originate from a slight canting of the Mn spins along the $[0001]$ direction.

Importantly, we found that such small in-plane field-induced change of chirality can persist up to room temperature. In Figure S12 (Supporting Information), we show the angular dependence of σ_{zy} measured at various temperatures with a fixed field of 1 T in the case of configuration I. With increasing of temperature, the σ_{zy} gradually decreases due to the temperature disturbance on the spin structure. In addition, the similar tendency of angu-

lar dependence AHC has also been observed in Mn_3Ge .^[29] We therefore can conclude that both the weak in-plane magnetization component and the direction of the applied magnetic field will not impact on the observed large AHE in $\text{Mn}_{2.4}\text{Ga}$.

2.5. Comparison of $\text{Mn}_{2.4}\text{Ga}$ with other AHE Materials

The zero-field AHC at various temperatures was extracted from the magnetic field dependence of the AHC by extrapolating the high magnetic field part back to zero field. As shown in Figure 5a, with decreasing temperature, the AHC shows a weaker dependence on the temperature, compared to the Mn_3Sn and Mn_3Ge .

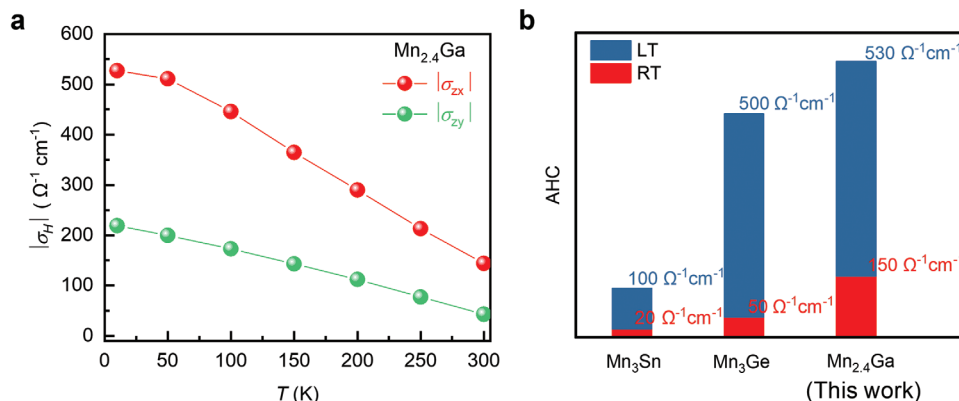


Figure 5. Summary of anomalous Hall conductivity of the $\text{Mn}_{2.4}\text{Ga}$. a) Temperature dependence of the AHC with two field and current configurations: $H||y, I||x$; $H||y, I||y$, respectively. b) The maximum AHC of the Mn_3X alloy (Sn, Ge, Ga)^[23,29] at room temperature (RT) and low temperature (LT), respectively.

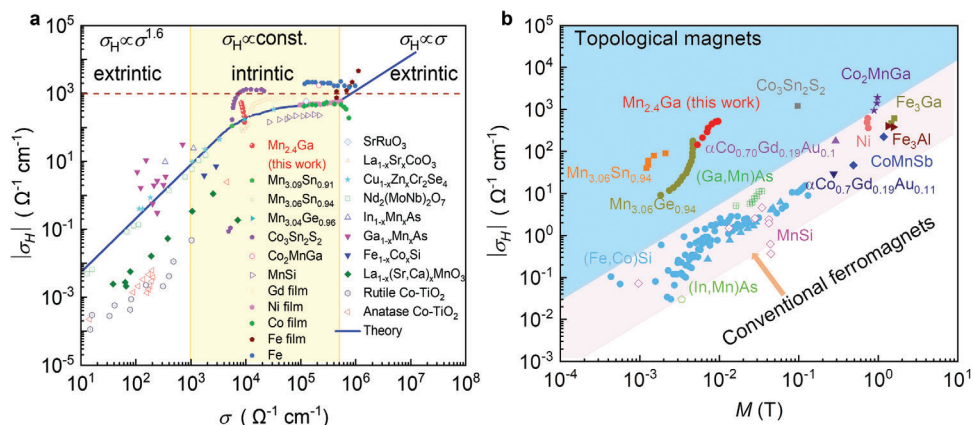


Figure 6. Comparison of $\text{Mn}_{2.4}\text{Ga}$ with other AHE materials. a) Relation between the Hall conductivity σ_H and the longitudinal conductivity σ of the $\text{Mn}_{2.4}\text{Ga}$ (10 to 300 K) plotted together with various ferromagnets, antiferromagnets, and transition metals (Ni, Gd, Fe, and Co thin films),^[61] Fe single crystals,^[61] $\text{Co}_3\text{Sn}_2\text{S}_2$,^[11] Mn_3Sn ,^[23] Mn_3Ge ,^[29] $\text{Mn}_3\text{Sn}_{0.94}$,^[30] Mn_3Co ,^[36] MnSi ,^[62] $\text{Fe}_{1-x}\text{Co}_x\text{Si}$,^[62] SrRuO_3 , $\text{La}_{1-x}\text{Sr}_x\text{CoO}_3$, $\text{La}_{1-x}(\text{SrCa})_x\text{MnO}_3$,^[63] $\text{Cu}_{1-x}\text{Zn}_x\text{Cr}_2\text{Se}_4$,^[63] $\text{Nd}_2(\text{MoNb})_2\text{O}_7$,^[63] and $\text{Ga}_{1-x}\text{Mn}_x\text{As}$, $\text{In}_{1-x}\text{Mn}_x\text{As}$, anatase- Co-TiO_2 , rutile- Co-TiO_2 .^[63] The yellow-shaded region marks the moderately dirty regime ($3 \times 10^3 \leq \sigma \leq 5 \times 10^5 \Omega^{-1} \text{cm}^{-1}$), in which the intrinsic Berry phase dominated the σ_H and nearly unchanged with σ . The super clean region of $\sigma \geq 5 \times 10^5 \Omega^{-1} \text{cm}^{-1}$, σ_H is mainly dominated by the extrinsic skew scattering. The poorly conducting regime $\sigma \leq 3 \times 10^3 \Omega^{-1} \text{cm}^{-1}$, the σ_H also originates from the extrinsic contribution, shows $\sigma_H \propto \sigma^{1.6}$ relation. The solid line presents the theoretical prediction.^[64] b) Full logarithmic plot of the magnetization (M) dependence of the AHC of $\text{Mn}_{2.4}\text{Ga}$, topological magnets,^[23,30,65] and conventional ferromagnets.^[18,36,66] The red shades mark the regions where σ_H is linearly related to M for conventional magnets. While the topological magnets surpass this linear relation and are located in the blue-shaded region.

Interestingly, the AHE caused by the Berry curvature should not depend on temperature, such as Fe_3Sn_2 ^[59] and $\text{Co}_3\text{Sn}_2\text{S}_2$.^[11] However, for the Kagome antiferromagnets, the AHE typically shows strong temperature dependence, including this work (Mn_3Ga) and previous work on Mn_3Sn ^[23] and Mn_3Ge .^[29] Although it is clear now that the Berry curvature generated by the triangular spin structure is crucial for the observed large AHE in these compounds, to the best of our knowledge, the origin of its temperature dependence remains an open question. In fact, the temperature-dependent intrinsic AHE has been discussed in the Ni films, which is related to the magnetocrystalline anisotropy changing with the temperature. As a result, the Fermi energy will pass through small band gaps caused by spin-orbital coupling.^[60] We then speculate that the triangular spin structure of $\text{Mn}_{2.4}\text{Ga}$ may be relatively insensitive to temperature, which is the response for the weak temperature-dependent intrinsic AHC observed in $\text{Mn}_{2.4}\text{Ga}$ single crystals. The AHC reaches a value of $\sigma_{zx} \approx 530 \Omega^{-1} \text{cm}^{-1}$ and $\sigma_{zy} \approx 220 \Omega^{-1} \text{cm}^{-1}$ at 10 K in x - z and y - z plane, respectively, which is quite high, especially for an antiferromagnet (Table S2, Supporting Information). More importantly, the large AHC of $\sigma_{zx} \approx 150 \Omega^{-1} \text{cm}^{-1}$ at 300K is remarkable because it surpasses the highest values observed in Mn_3Sn ($\approx 20 \Omega^{-1} \text{cm}^{-1}$) and Mn_3Ge ($\approx 50 \Omega^{-1} \text{cm}^{-1}$) at room temperature (Figure 5b).

To further scale the transport properties of the $\text{Mn}_{2.4}\text{Ga}$, we have summarized the relation between the σ_H and the σ together with some reported AHE materials (Figure 6a). The longitudinal σ of $\text{Mn}_{2.4}\text{Ga}$ is in the range of $5 \times 10^3 \Omega^{-1} \text{cm}^{-1}$ indicating the AHE is mainly governed by the intrinsic mechanism like Mn_3Sn and Mn_3Ge . This is also in line with the theoretical calculations.^[36,55] For topological antiferromagnets, in addition to the large AHE, other topological transport properties like ANE, large magnetoconductivity, and PHE have all been observed in Mn_3Sn and Mn_3Ge . These properties are attributed to the large

Berry curvature stemming from the Weyl points, which is not related to the net magnetization.^[36] It can be seen that the $\text{Mn}_{2.4}\text{Ga}$ shows an obviously dependent on the σ . The σ is temperature dependent. As we mentioned above, the temperature perturbation noncollinear antiferromagnetic structure will result in the temperature-dependent intrinsic AHC as well as the σ dependent intrinsic AHC.

Finally, the magnetization dependence of the σ_H of the Mn_3X alloys and other ferromagnetic materials is plotted in Figure 6b. We note that the $\text{Mn}_{2.4}\text{Ga}$ presented in this work is located in the blue region where the σ_H is beyond the linear relation for the conventional magnets (pink region). On the other hand, the well-known topological materials $\text{Co}_3\text{Sn}_2\text{S}_2$ and Co_2MnGa are also in this regime that have been revealed the evidence of the Weyl fermions by ARPES,^[11,67,68] as well as the Mn_3Sn .^[8] Moreover, the large positive magnetoconductivity of Mn_3Ge indicates that the Mn_3Ge may be also a topological magnet.^[36] The present results strongly suggest that kagome-based antiferromagnets, including but not limited to the Mn_3X ($X = \text{Sn}, \text{Ge}, \text{Ga}$) family, are worthy of further investigation for large AHE.

3. Conclusion

We have demonstrated on the first experimental realization of the long-sought-after last member of the Mn_3X kagome antiferromagnet family, the off-stoichiometry Mn_3Ga in the form of single crystals, which shows large AHE at room temperature. By tuning the Fermi level close to the Weyl points, we found the non-stoichiometric $\text{Mn}_{2.4}\text{Ga}$ single crystal exhibits strikingly large AHC of $\approx 150 \Omega^{-1} \text{cm}^{-1}$ at room temperature and $\approx 530 \Omega^{-1} \text{cm}^{-1}$ at 10 K, despite a very small magnetization $\approx 0.05 \mu_B$ per formula unit in the kagome plane. The results of the angular dependence of the AHE further confirm that the small residual in-plane magnetization has no impact on the observed Hall

response apart from controlling the chirality of the triangular spin structure. Our band structure calculations indicate that the large AHE in $\text{Mn}_{2.4}\text{Ga}$ originates from a significantly enhanced Berry curvature associated with tuning the Fermi level close to the Weyl points. In addition, we have fabricated the Mn_{3-x}Ga ($x = 0.2, 0.3, 0.4, 0.5, 0.6, 0.65$) polycrystalline samples and magnetic and transport results clearly indicate they exhibit a layered kagome antiferromagnetic structure with a tunable magnetic and AHE (Figure S13, Supporting Information), which demonstrates the efficient Fermi level engineering via off-stoichiometric substitutional alloying. We thus suggest that, by changing the composition of Mn, a precise tuning of the E_F may be realized, which will further enhance the value of AHC even at room temperature. In this sense, the Fermi-level-tuned Mn_{3-x}Ga can be a new paradigm of the field-controlled antiferromagnetic family with promising prospects for future spintronics.

4. Experimental Section

Sample Preparation: Single crystals of $\text{Mn}_{2.4}\text{Ga}$ were prepared by Pb flux method. First, the bulk polycrystalline $\text{Mn}_{2.4}\text{Ga}$ was prepared by arc melting method with high-purity Mn (99.99 wt%) and Ga (99.99 wt%) under an argon atmosphere. Second, a polycrystalline sample and Pb with the molar ratio of Mn:Ga:Pb = 2.4:1:22.5 were placed in an Al_2O_3 crucible that was sealed in quartz tubes later. Then the quartz tubes were slowly heated to 1423 K and held on for 2 days in an electric furnace. The quartz tube was subsequently cooled down to 1023 K at a rate of 4 K h^{-1} to reach the low-temperature phase region. After that the quartz tubes were cooled down to the 953 K at a rate of 2 K h^{-1} . Finally, the quartz tubes were moved into a centrifuge to separate the Pb flux from the isolated single crystals at 953 K.

The Mn_{3-x}Ga polycrystals were prepared by the melt-spinning method. Details could be found in the previous work.^[50]

The single crystals of Mn_3Sn were prepared by Sn self-flux method. The high purity of Mn (99.99%) and Sn (99.99%) were mixed with an atomic ratio of Mn:Sn = 7:3 and placed in an alumina crucible. The sealed quartz tubes were heated to 1423 K and held on for 24 h. Then the quartz tubes were cooled down to 1273 K at a rate of 25 K h^{-1} . After that, the quartz tubes were cooled down to 1173 K at a rate of 1 K h^{-1} . Finally, the quartz tubes were moved into a centrifuge to separate the Sn flux from the isolated single crystals at 1173 K.

Structural and Composition Characterizations: The crystal structure and orientation of the as-grown single crystals were determined using single-crystal X-ray diffraction (RAPID, Rigaku) at room temperature. The lattice parameters were calculated by Rietveld refinement. All the samples were shown to be in a single phase and the lattice parameters were agree with previous reports. Based on the energy-dispersive X-ray analysis with a scanning electron microscope, the composition of single crystals was determined to be $\text{Mn}_{2.4}\text{Ga}$.

Magnetization Characterizations: The magnetization measurements were carried out using a commercial SQUID magnetometer (MPMS, Quantum Design) equipped with a high-temperature module in the temperature range of 2K–800 K. The high magnetic field experiments were carried out using a Physical Property Measurement System (PPMS, Quantum Design) with a maximum applied magnetic field 16 T.

Device Fabrication: First, thin flakes with different orientations were fabricated from the single crystal of $\text{Mn}_{2.4}\text{Ga}$ using a focused ion-beam system (Helions PFIB CXe). Second, the thin flakes were then transferred to a copper chip by the tungsten needle to further reduce the thickness of the flakes to $\approx 1\ \mu\text{m}$. Third, the thin flakes were transferred to the silicon wafer with pre-made electrodes. Finally, the electrodes and the flake were connected by the plating Pt. Mn_3Sn devices were fabricated using a similar procedure.

Transport Measurements: The longitudinal and Hall resistivity of devices were measured simultaneously in standard five-probe geometry by using a commercial PPMS system (Quantum Design). In order to eliminate the influence of probe misalignment, the Hall contributions to the longitudinal resistivity were eliminated by adding and subtracting the resistivity data taken at positive and negative magnetic fields.

First Principle Calculations: Calculations were conducted using density functional theory (DFT) implemented in the Vienna ab initio simulation package^[69] (VASP) code. The exchange correlation functional was the Generalized-Gradient-Approximation^[70] (GGA) of the Perdew–Burke–Ernzerhof^[71] (PBE) functional. The cutoff energy was set as 450 eV, energy and force convergence criteria were set as 10^{-5} eV and 0.01 eV \AA^{-1} . Spin-orbit coupling (SOC) was included in all calculations. $\text{Mn}_{2.43}\text{Ga}$ was built by considering a $3 \times 3 \times 1$ Mn_3Ga supercell and replacing three Mn atoms with Ga randomly. The Mn magnetic moment was $\approx 3\ \mu_B$ for Mn_3Ga and $2.4\ \mu_B$ for $\text{Mn}_{2.43}\text{Ga}$, these calculated values agree well with the experimental results. The anomalous Hall conductivity and Berry curvature were calculated in the Wannier90^[72,73] and Wannier tools package.^[74]

Supporting Information

Supporting Information is available from the Wiley Online Library or from the author.

Acknowledgements

This work was supported by the National Key R&D Program of China (No. 2022YFA1402600), the National Natural Science Foundation of China (Grants No. 12204347, 12274438, 12274321 and 12074415), and the Beijing Natural Science Foundation (Grant No. Z230006). A portion of this work was carried out at the Synergetic Extreme Condition User Facility (SECUF).

Conflict of Interest

L.X.S., H.L., X.K.X., Y.-C. Lau, and W.H.W. have filed a patent on the growth of the single crystal and the anomalous Hall effect in $\text{Mn}_{2.4}\text{Ga}$. The authors declare no conflict of interest.

Author Contributions

Y.-C.L. and W.H.W. conceived the idea and supervised the project. L.X.S. carried out the preparation of the samples and conducted the structure, magnetic, and transport measurements. L.X.S. and X.L. fabricated the Hall devices. B.D., Y.Y., and H.L. performed the LTEM and STEM experiments. F.Z. and H.L. performed the ab initio calculation. All authors discussed the results and contributed to the manuscript preparation.

Data Availability Statement

The data that support the findings of this study are available from the corresponding author upon reasonable request.

Keywords

anomalous Hall effect, kagome lattice, Mn_3Ga , noncollinear antiferromagnets

Received: January 3, 2024
Revised: February 14, 2024
Published online:

- [1] L. Balents, *Nature* **2010**, 464, 199.
- [2] Q. Chen, S. C. Bae, S. Granick, *Nature* **2011**, 469, 381.
- [3] S. Yan, D. A. Huse, S. R. White, *Science* **2011**, 332, 1173.
- [4] T. H. Han, J. S. Helton, S. Chu, D. G. Nocera, J. A. Rodriguez-Rivera, C. Broholm, Y. S. Lee, *Nature* **2012**, 492, 406.
- [5] G. Xu, B. Lian, S. C. Zhang, *Phys. Rev. Lett.* **2015**, 115, 186802.
- [6] H. Zhao, H. Li, B. R. Ortiz, S. M. L. Teicher, T. Park, M. Ye, Z. Wang, L. Balents, S. D. Wilson, I. Zeljkovic, *Nature* **2021**, 599, 216.
- [7] L. Nie, K. Sun, W. Ma, D. Song, L. Zheng, Z. Liang, P. Wu, F. Yu, J. Li, M. Shan, D. Zhao, S. Li, B. Kang, Z. Wu, Y. Zhou, K. Liu, Z. Xiang, J. Ying, Z. Wang, T. Wu, X. Chen, *Nature* **2022**, 604, 59.
- [8] K. Kuroda, T. Tomita, M. T. Suzuki, C. Bareille, A. A. Nugroho, P. Goswami, M. Ochi, M. Ikhlas, M. Nakayama, S. Akebi, R. Noguchi, R. Ishii, N. Inami, K. Ono, H. Kumigashira, A. Varykhalov, T. Muro, T. Koretsune, R. Arita, S. Shin, T. Kondo, S. Nakatsuji, *Nat. Mater.* **2017**, 16, 1090.
- [9] Z. Hou, W. Ren, B. Ding, G. Xu, Y. Wang, B. Yang, Q. Zhang, Y. Zhang, E. Liu, F. Xu, W. Wang, G. Wu, X. Zhang, B. Shen, Z. Zhang, *Adv. Mater.* **2017**, 29, 1701144.
- [10] J. X. Yin, S. S. Zhang, H. Li, K. Jiang, G. Chang, B. Zhang, B. Lian, C. Xiang, I. Belopolski, H. Zheng, T. A. Cochran, S. Y. Xu, G. Bian, K. Liu, T. R. Chang, H. Lin, Z. Y. Lu, Z. Wang, S. Jia, W. Wang, M. Z. Hasan, *Nature* **2018**, 562, 91.
- [11] E. Liu, Y. Sun, N. Kumar, L. Muchler, A. Sun, L. Jiao, S. Y. Yang, D. Liu, A. Liang, Q. Xu, J. Kroder, V. Suss, H. Borrmann, C. Shekhar, Z. Wang, C. Xi, W. Wang, W. Schnelle, S. Wirth, Y. Chen, S. T. B. Goennenwein, C. Felser, *Nat. Phys.* **2018**, 14, 1125.
- [12] J.-X. Yin, S. S. Zhang, G. Chang, Q. Wang, S. S. Tsirkin, Z. Guguchia, B. Lian, H. Zhou, K. Jiang, I. Belopolski, N. Shumiya, D. Multer, M. Litskevich, T. A. Cochran, H. Lin, Z. Wang, T. Neupert, S. Jia, H. Lei, M. Z. Hasan, *Nat. Phys.* **2019**, 15, 443.
- [13] P. P. Provenzano, *Nat. Mater.* **2020**, 19, 130.
- [14] M. H. Christensen, X. Wang, Y. Schattner, E. Berg, R. M. Fernandes, *Phys. Rev. Lett.* **2020**, 125, 247001.
- [15] X. Teng, L. Chen, F. Ye, E. Rosenberg, Z. Liu, J. X. Yin, Y. X. Jiang, J. S. Oh, M. Z. Hasan, K. J. Neubauer, B. Gao, Y. Xie, M. Hashimoto, D. Lu, C. Jozwiak, A. Bostwick, E. Rotenberg, R. J. Birgeneau, J. H. Chu, M. Yi, P. Dai, *Nature* **2022**, 609, 490.
- [16] E. H. Hall, *Proc. Phys. Soc.* **1880**, 4, 325.
- [17] C. M. Hurd, C. Chien, C. Westgate, Plenum, New York **1980**, 1, <https://doi.org/10.1007/978-1-4757-1367-1>.
- [18] N. Nagaosa, J. Sinova, S. Onoda, A. H. MacDonald, N. P. Ong, *Rev. Mod. Phys.* **2010**, 82, 1539.
- [19] Y. Machida, S. Nakatsuji, S. Onoda, T. Tayama, T. Sakakibara, *Nature* **2010**, 463, 210.
- [20] H. Ishizuka, Y. Motome, *Phys. Rev. B* **2013**, 87, 081105.
- [21] H. Chen, Q. Niu, A. H. MacDonald, *Phys. Rev. Lett.* **2014**, 112, 017205.
- [22] J. Kübler, C. Felser, *Europhys. Lett.* **2014**, 108, 67001.
- [23] S. Nakatsuji, N. Kiyohara, T. Higo, *Nature* **2015**, 527, 212.
- [24] M. Kimata, H. Chen, K. Kondou, S. Sugimoto, P. K. Muduli, M. Ikhlas, Y. Omori, T. Tomita, A. H. MacDonald, S. Nakatsuji, Y. Otani, *Nature* **2019**, 565, 627.
- [25] T. Higo, K. Kondou, T. Nomoto, M. Shiga, S. Sakamoto, X. Chen, D. Nishio-Hamane, R. Arita, Y. Otani, S. Miwa, S. Nakatsuji, *Nature* **2022**, 607, 474.
- [26] M. Ikhlas, S. Dasgupta, F. Theuss, T. Higo, S. Kittaka, B. J. Ramshaw, O. Tchernyshyov, C. W. Hicks, S. Nakatsuji, *Nat. Phys.* **2022**, 18, 1086.
- [27] X. Li, J. Koo, Z. Zhu, K. Behnia, B. Yan, *Nat. Commun.* **2023**, 14, 1642.
- [28] N. Kiyohara, T. Tomita, S. Nakatsuji, *Phys. Rev. Appl.* **2016**, 5, 064009.
- [29] A. K. Nayak, J. E. Fischer, Y. Sun, B. Yan, J. Karel, A. C. Komarek, C. Shekhar, N. Kumar, W. Schnelle, J. Kübler, C. Felser, S. S. P. Parkin, *Sci. Adv.* **2016**, 2, e1501870.
- [30] M. Ikhlas, T. Tomita, T. Koretsune, M.-T. Suzuki, D. Nishio-Hamane, R. Arita, Y. Otani, S. Nakatsuji, *Nat. Phys.* **2017**, 13, 1085.
- [31] T. Higo, H. Man, D. B. Gopman, L. Wu, T. Koretsune, O. M. J. van 't Erve, Y. P. Kabanov, D. Rees, Y. Li, M. T. Suzuki, S. Patankar, M. Ikhlas, C. L. Chien, R. Arita, R. D. Shull, J. Orenstein, S. Nakatsuji, *Nat. Photonics* **2018**, 12, 73.
- [32] C. Wuttke, F. Caglieris, S. Sykora, F. Scaravaggi, A. U. B. Wolter, K. Manna, V. Süß, C. Shekhar, C. Felser, B. Büchner, C. Hess, *Phys. Rev. B* **2019**, 100, 085111.
- [33] P. K. Rout, P. P. Madduri, S. K. Manna, A. K. Nayak, *Phys. Rev. B* **2019**, 99, 094430.
- [34] L. Xu, X. Li, L. Ding, K. Behnia, Z. Zhu, *Appl. Phys. Lett.* **2020**, 117, 222403.
- [35] M. Wu, H. Isshiki, T. Chen, T. Higo, S. Nakatsuji, Y. Otani, *Appl. Phys. Lett.* **2020**, 116, 132408.
- [36] T. Chen, T. Tomita, S. Minami, M. Fu, T. Koretsune, M. Kitatani, I. Muhammad, D. Nishio-Hamane, R. Ishii, F. Ishii, R. Arita, S. Nakatsuji, *Nat. Commun.* **2021**, 12, 572.
- [37] Y. Pan, C. Le, B. He, S. J. Watzman, M. Yao, J. Gooth, J. P. Heremans, Y. Sun, C. Felser, *Nat. Mater.* **2022**, 21, 203.
- [38] D. F. Zhang, J. K. Liang, *Acta Phys. Sin.* **1966**, 22, 1005.
- [39] E. Krén, G. Kádár, *Solid State Commun.* **1970**, 8, 1653.
- [40] H. Niida, T. Hori, Y. Nakagawa, *J. Phys. Soc.* **1983**, 52, 1512.
- [41] H. Niida, T. Hori, Y. Yamaguchi, Y. Nakagawa, *J. Appl. Phys.* **1993**, 73, 5692.
- [42] H. Niida, T. Hori, H. Onodera, Y. Yamaguchi, Y. Nakagawa, *J. Appl. Phys.* **1996**, 79, 5946.
- [43] B. Balke, G. H. Fecher, J. Winterlik, C. Felser, *Appl. Phys. Lett.* **2007**, 90, 152504.
- [44] P. Kharel, Y. Huh, N. Al-Aqtash, V. R. Shah, R. F. Sabirianov, R. Skomski, D. J. Sellmyer, *J. Phys.:Condens. Matter* **2014**, 26, 126001.
- [45] J. Z. Wei, R. Wu, Y. B. Yang, X. G. Chen, Y. H. Xia, Y. C. Yang, C. S. Wang, J. B. Yang, *J. Appl. Phys.* **2014**, 115.
- [46] Z. Jiao, Z. Fu, J. Wang, R. Zhang, C. Jiang, *J. Magn. Magn. Mater.* **2019**, 489, 165308.
- [47] L. X. Song, B. Ding, H. Li, S. H. Lv, Y. Yao, D. L. Zhao, J. He, W. H. Wang, *J. Magn. Magn. Mater.* **2021**, 536, 168109.
- [48] L. X. Song, B. Ding, H. Li, S. H. Lv, Y. Yao, D. L. Zhao, J. He, W. H. Wang, *Appl. Phys. Lett.* **2021**, 119, 152405.
- [49] X. Zhao, J. Zhao, *Adv. Mater. Interfaces* **2022**, 9, 2201606.
- [50] L. Song, W. Li, S. Lv, X. Xi, D. Zhao, J. He, W. Wang, *J. Appl. Phys.* **2022**, 131, 173903.
- [51] G. Kirste, J. Freudenberger, S. Wurmehl, *Acta Mater.* **2023**, 258, 119205.
- [52] K. Minakuchi, R. Y. Umetsu, K. Ishida, R. Kainuma, *J. Alloys Compd.* **2012**, 537, 332.
- [53] Z. H. Liu, Y. J. Zhang, G. D. Liu, B. Ding, E. K. Liu, H. M. Jafri, Z. P. Hou, W. H. Wang, X. Q. Ma, G. H. Wu, *Sci. Rep.* **2017**, 7, 515.
- [54] H. Guo, Z. Feng, H. Yan, J. Liu, J. Zhang, X. Zhou, P. Qin, J. Cai, Z. Zeng, X. Zhang, X. Wang, H. Chen, H. Wu, C. Jiang, Z. Liu, *Adv. Mater.* **2020**, 32, 2002300.
- [55] Y. Zhang, Y. Sun, H. Yang, J. Železný, S. P. P. Parkin, C. Felser, B. Yan, *Phys. Rev. B* **2017**, 95, 075128.
- [56] V. Rai, S. Jana, M. Meven, R. Dutta, J. Perßon, S. Nandi, *Phys. Rev. B* **2022**, 106, 195114.
- [57] T. Nagamiya, S. Tomiyoshi, Y. Yamaguchi, *Solid State Commun.* **1982**, 42, 385.
- [58] S. Tomiyoshi, *J. Phys. Soc. Jpn.* **1982**, 51, 803.
- [59] L. Ye, M. Kang, J. Liu, F. von Cube, C. R. Wicker, T. Suzuki, C. Jozwiak, A. Bostwick, E. Rotenberg, D. C. Bell, L. Fu, R. Comin, J. G. Checkelsky, *Nature* **2018**, 555, 638.
- [60] L. Ye, Y. Tian, X. Jin, D. Xiao, *Phys. Rev. B* **2012**, 85, 220403.
- [61] T. Miyasato, N. Abe, T. Fujii, A. Asamitsu, S. Onoda, Y. Onose, N. Nagaosa, Y. Tokura, *Phys. Rev. Lett.* **2007**, 99, 086602.
- [62] N. Manyala, Y. Sidis, J. F. DiTusa, G. Aeppli, D. P. Young, Z. Fisk, *Nat. Mater.* **2004**, 3, 255.

- [63] S. Onoda, N. Sugimoto, N. Nagaosa, *Phys. Rev. B* **2008**, *77*, 165103.
- [64] S. Onoda, N. Sugimoto, N. Nagaosa, *Phys. Rev. Lett.* **2006**, *97*, 126602.
- [65] A. Sakai, Y. P. Mizuta, A. A. Nugroho, R. Sihombing, T. Koretsune, M.-T. Suzuki, N. Takemori, R. Ishii, D. Nishio-Hamane, R. Arita, P. Goswami, S. Nakatsuji, *Nat. Phys.* **2018**, *14*, 1119.
- [66] S. Nakatsuji, *AAPPS Bull.* **2022**, *32*, 25.
- [67] I. Belopolski, K. Manna, D. S. Sanchez, G. Chang, B. Ernst, J. Yin, S. S. Zhang, T. Cochran, N. Shumiya, H. Zheng, B. Singh, G. Bian, D. Multer, M. Litskevich, X. Zhou, S. M. Huang, B. Wang, T. R. Chang, S. Y. Xu, A. Bansil, C. Felser, H. Lin, M. Z. Hasan, *Science* **2019**, *365*, 1278.
- [68] D. F. Liu, A. J. Liang, E. K. Liu, Q. N. Xu, Y. W. Li, C. Chen, D. Pei, W. J. Shi, S. K. Mo, P. Dudin, T. Kim, C. Cacho, G. Li, Y. Sun, L. X. Yang, Z. K. Liu, S. S. P. Parkin, C. Felser, Y. L. Chen, *Science* **2019**, *365*, 1282.
- [69] G. Kresse, J. Furthmüller, *Phys. Rev. B* **1996**, *54*, 11169.
- [70] J. P. Perdew, K. Burke, M. Ernzerhof, *Phys. Rev. Lett.* **1996**, *77*, 3865.
- [71] J. P. Perdew, K. Burke, M. Ernzerhof, *Phys. Rev. Lett.* **1998**, *80*, 891.
- [72] A. A. Mostofi, J. R. Yates, G. Pizzi, Y.-S. Lee, I. Souza, D. Vanderbilt, N. Marzari, *Comput. Phys. Commun.* **2014**, *185*, 2309.
- [73] A. A. Mostofi, J. R. Yates, Y.-S. Lee, I. Souza, D. Vanderbilt, N. Marzari, *Comput. Phys. Commun.* **2008**, *178*, 685.
- [74] Q. Wu, S. Zhang, H.-F. Song, M. Troyer, A. A. Soluyanov, *Comput. Phys. Commun.* **2018**, *224*, 405.